First-principles study of the surfaces of zirconia

A. Christensen* and Emily A. Carter†
Department of Chemistry and Biochemistry, Box 951569, University of California, Los Angeles, California 90095-1569
(Received 24 February 1998)

We have studied the surfaces of zirconia (ZrO_2) by first-principles calculations using density functional theory. We predict surface energies and relaxations for the principal surfaces of different bulk phases of zirconia. We find that the stoichiometric tetragonal(111) and monoclinic(111) are the most stable surfaces. We find a strong linear correlation between surface energies before and after relaxing the surface ions. Our predicted surface energies also provide insight into the tetragonal-monoclinic phase transition in small ZrO_2 particles. [S0163-1829(98)07635-8]

I. INTRODUCTION

Zirconia (ZrO_2) is an important ceramic material with an increasing range of applications, where surface properties are important, e.g., for thin-film coatings[1] and catalysis.[2–5] Very recently nanotube structures of zirconia have also been synthesized,[6] which may allow ZrO_2 to be used in, e.g., microelectromechanical systems someday.

A great deal of experimental data for zirconia surfaces, including Auger, photoelectron, and vibrational spectroscopies as well as electron microscopies and x-ray diffraction, have been reported.[7–15] However, these data only provide indirect and incomplete information about the detailed surface atomic structure. Also the interpretation of many experimental studies are often complicated by finite-size effects because samples have granular, often polymorphic, fine structure and the presence of dopants like Y_2O_3, which is known to segregate to the surface.[16–18,9] Furthermore comparison is often difficult due to different experimental conditions and methods of preparation.

Due to the structural complexity of the material, much less theoretical work on the ZrO_2 surfaces has appeared in the literature. To our knowledge, the only reported *ab initio* study on ZrO_2 surfaces is Ref. 19, which investigated the tetragonal(001) surface using the Hartree-Fock method for periodic slabs. The bulk properties of zirconia have been examined using both density functional methods[20–23] and semiempirical modeling combined with *ab initio* techniques.[24–26] We defer discussion of previous theoretical and experimental results until appropriate points of comparison in the text.

In this paper, we have studied the surfaces of zirconia for all experimentally observed bulk phases at low pressure. We report surface energies and local ionic relaxations near the surface. Surface energies of solid metal oxides are notoriously difficult to measure,[27] but a few results have been reported for zirconia at high temperatures, using the multiphase equilibration technique for the measurement of contact angles.[30,31]

In Fig. 1 we show the crystalline unit cells of the three bulk phases of zirconia observed at low pressure. From 0 to 1180 °C, the stable phase is the McCullough-Trueblood structure,[32] which has monoclinic symmetry ($P2_1/c$) and sevenfold cation coordination. This structure is often referred to as baddeleyite in mineralogical contexts. From 1180 to 2370 °C, the stable phase has tetragonal symmetry ($P4_2/nmc$) (Ref. 33) and eightfold cation coordination. From 2370 °C to the melting temperature (2600 °C), the stable phase is fluorite, which has full cubic symmetry ($Fm3m$) (Ref. 34) and also eightfold cation coordination. The difference between the cubic and tetragonal structure is the alternating distortion of the O-atom columns along the 4_2 axes, as indicated in Fig. 1(b) by arrows. We refer to this as the *t* distortion in the rest of this paper. The magnitude of the *t* distortion is given by the ratio $d_z=\Delta z/c$, where Δz is the O-atom displacement along the *c* axis. By adding Y_2O_3 or certain other metal oxides, it is possible to stabilize the tetragonal phase at room temperature. Throughout this paper, the letters *c*, *t*, and *m* refer to the cubic, tetragonal, and monoclinic phases, respectively, of zirconia.

Also listed in Fig. 1 are the structurally unique surfaces for each of these three bulk phases. The main focus of this paper is to explore the stability and reconstructions of each of these surfaces in order to offer a more complete understanding of the ZrO_2 surfaces than has been possible from experiments alone to date.

This paper is organized as follows. In Sec. II, we outline calculational details and tests of the pseudopotential used in this study. In Sec. III, we discuss principles of guessing stable bulk terminations and choices of computational parameters in our study. In Sec. IV, we present and discuss the results of our calculations. In Sec. V, we draw some general conclusions.

II. COMPUTATIONAL ASPECTS

We have performed first-principles calculations within the local density (LDA) and pseudopotential approximations to density functional theory (DFT), using the computer code CASTEP,[35] which solves the Kohn-Sham equations using a plane-wave expansion for electronic charge density and wave functions. We have chosen to study the zirconia system using this method, because it has proven remarkably successful in predicting ground-state bulk and surface properties for a wide range of materials, including transition metal oxides. At first sight one might think that the notorious overbinding of the LDA would lead to a systematic overestimation of surface energies, but an extended study for elemental metals across the Periodic Table has shown that this is not the case.[36,37] Furthermore, ZrO_2 does not belong to the class of strongly correlated metal oxides such as NiO, where the LDA is known to fail.[38] Oxides where the metal cation has a

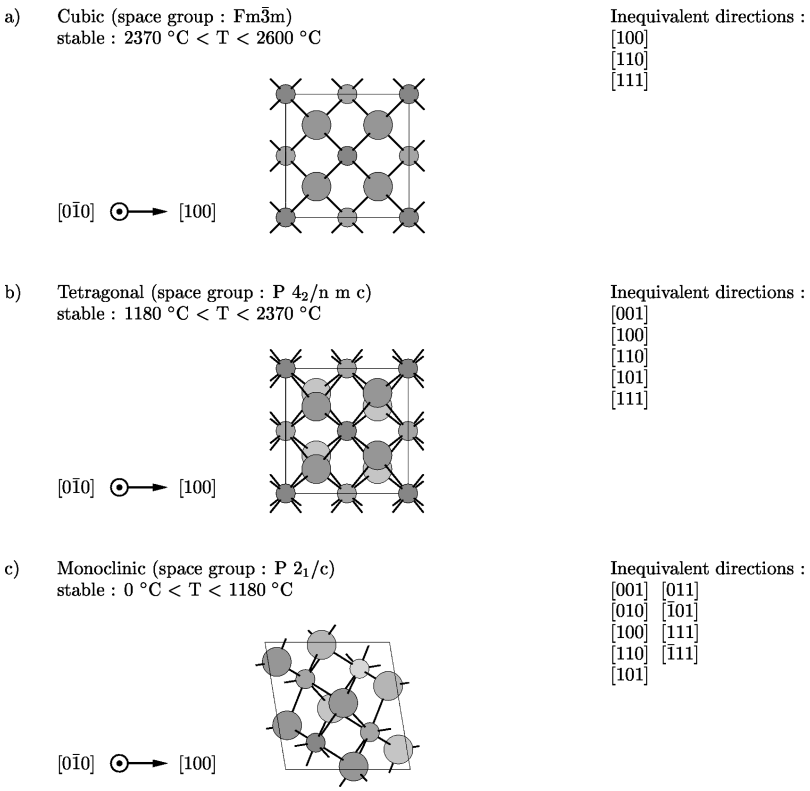

FIG. 1. Unit cells of the observed bulk structures of ZrO_2. The *c* and *t* unit cells chosen correspond to the CaF_2 unit cell, to which we refer crystalline directions, indicated by arrows at the lower right of each panel. Zr ions are small and O ions are large. Ions in the foreground are shaded darker than ions in the background.

nominal d^0 valence configuration generally will not display strong valence correlation effects[39] and consequently are expected to be well described by the LDA or the generalized gradient approximation (GGA).

All calculations presented in this paper have been performed spin restricted, that is the spin density is taken to vanish everywhere. Our preliminary calculations have indicated that including freedom for spatial variations in the spin density has negligible effects, as should be expected for a solid with predominantly (~80%) ionic bonding character.[40,20,41,23]

A. The pseudopotential

We have used the scheme of Troullier and Martins[42] to generate norm conserving pseudopotentials,[43] using the Ceperley and Alder exchange correlation potential[44] as parametrized by Perdew and Zunger.[45] The generated pseudopotentials were cast into the separable form of Kleinman and Bylander.[46]

For Zr, we have used the cutoff radii $r_s=1.59$ Å, $r_p=2.06$ Å, and $r_d=0.78$ Å, respectively, in its neutral atomic ground-state configuration $[\mathrm{Kr}]4d^2 5s^2$. These radii correspond to where 90% of the pseudocharge is encapsulated for the corresponding *l* channel, which is the standard choice in the Troullier and Martins scheme. The *p* pseudocore radii are relatively large and will inevitably overlap somewhat with O projectors, which in principle could lead to inaccuracies. However, the Zr core size is difficult to reduce due to the 4*s*, 4*p* core levels lying close to the valence levels; we have performed many tests for various ZrO_2 structures, which are presented in Secs. II B and III B, and we are confident that the errors due to projector overlap are insignificant in this oxide material. A very accurate description of the energetics in a Zr crystal requires inclusion of the (4*s*,4*p*) core states, which are rather extended and overlap slightly with (4*s*,4*p*) core states at neighboring Zr atoms. However, in ZrO_2, Zr ions only have O ions as nearest neighbors and consequently the Zr(4*s*,4*p*) states can only hybridize with O states. In ZrO_2, all O resonances are well separated in energy from the Zr(4*s*,4*p*) resonances[21] and therefore the O-Zr(4*s*,4*p*) hybridization is weak. Thus we expect the frozen core approximation, which is the basis for the pseudopotential representation, to be accurate for ZrO_2, even if the Zr(4*s*,4*p*) states are treated as core states.

For O, we have used the cutoff radii $r_s=0.90$ Å and $r_p=1.06$ Å, respectively, in its neutral atomic ground-state configuration $[\mathrm{He}]2s^2 2p^4$. These choices for cutoff radii for oxygen are slightly larger than used in related recent studies[47–50] involving metal oxides. Our motivation for choosing these slightly larger cutoff radii is to achieve convergence of the plane-wave expansion of wave functions using a reasonable kinetic energy cutoff — no fitting whatsoever has influenced these choices. Using our pseudopotentials for zirconia, the total energy is approximately 0.03 eV/atom above absolute convergence at a kinetic energy cutoff at 700 eV. This level of absolute convergence is sufficient, since we are only concerned with energy differences, which converges faster than absolute total energies. In the following we will refer to this as pseudopotential set *(A)*, which is the pseudopotential on which we will base the rest

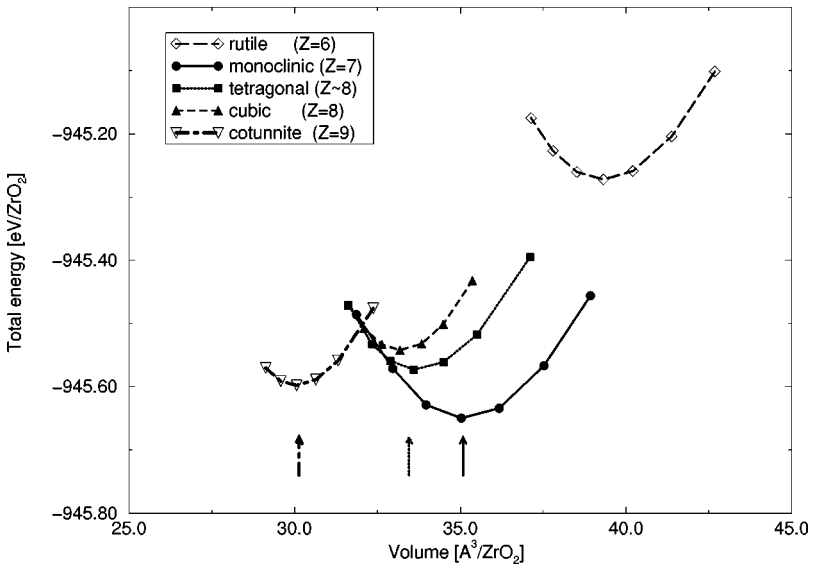

FIG. 2. Calculated cohesive energy curves using our Troullier-Martins pseudopotential *(A)* for competing bulk phases of zirconia at $T=0$, obtained by full (unit cell and intracellular) structural relaxation. Arrows show experimental volumes extrapolated to $T=0$. Z is the coordination number of Zr in the structure.

of our study. We would like to emphasize that relaxing the cutoff radii should generally be done with caution.

In the testing phase of this study, we have also used a harder O pseudopotential for checking the sensitivity of our results to the choice of cutoff radii. This pseudopotential — which we refer to as *(B)* in the following — is again generated using the Troullier and Martins scheme, but with smaller, more conservatively chosen cutoff radii, $r_s=r_p=0.69$ Å. These cutoff radii are consistent with those used in related studies of metal oxides.[47–50] For Zr, the same pseudopotential is used as in set *(A)*, described above. Of course, a significantly higher kinetic energy cutoff is needed to converge total energies using this pseudopotential.

We have also tested the Zr and O pseudopotentials recommended for oxides in the CERIUS^2 software package.[51] We will refer to this as pseudopotential set *(C)* in the following. These pseudopotentials are generated by the Lin procedure[52] and subsequently cast into the Kleinman-Bylander form. For Zr, the *s* and *d* projectors are generated using the ground-state atomic configuration $[\mathrm{Kr}]4d^2 5s^2$ and cutoff radii $r_s=1.43$ Å and $r_d=1.32$ Å for the *s* and *d* channels, respectively. The *p* projector is generated using the excited, ionic atomic configuration $[\mathrm{Kr}]4d^2 5s^{0.75} 5p^{0.25}$ and cutoff radius $r_p=1.43$ Å. The O *s* and *p* projectors are generated using the ground-state atomic configuration $[\mathrm{He}]2s^2 2p^4$ and cutoff radius $r_{sp}=0.95$ Å for both channels whereas the *d* projector is generated using the excited, ionic configuration $[\mathrm{He}]2s^1 2p^{1.75} 3d^{0.25}$ and cutoff radius $r_d=0.95$ Å. Pseudopotential set *(C)* is softer than pseudopotential set *(A)* and reaches a similar level of total energy convergence at ~50–100 eV lower kinetic energy cutoff.

We will demonstrate in Secs. II B and III B that our pseudopotential *(A)* gives results in agreement with other calculations and experimental data, indicating a sufficient transferability within the scope of our study.

B. The bulk phases of zirconia

In this section we present calculations of the cohesive energy curves as a function of volume for competing bulk phases having AB_2 stoichiometry but different coordination numbers and symmetry, using the pseudopotential *(A)* described above. In Fig. 2 we show the cohesive energy curves at $T=0$ for bulk phases with cation coordination numbers ranging from 6 to 9 anions.

Each structure has been relaxed with respect to all unit cell (lattice constants *a*, *b*, *c* and cell angles α,β,γ) and intracell degrees of freedom consistent with the space group of the structure. These calculations have been performed with a plane-wave cutoff at 800 eV, where energy differences are fully converged, and with a *k*-point sampling spacing of 0.05 Å^{-1}. All the structures considered are insulators around their equilibrium volumes, allowing for larger *k*-point sampling spacing than in the case of metals. By decreasing the sampling spacing, we estimated the *k*-point integration error to be less than 1 meV/atom. At this kinetic energy cutoff and *k*-point sampling, the Pulay stresses are very small and the Pulay stress correction[53] is vanishing (less than 0.01 meV/atom). The cohesive energy curves have been mapped out by applying positive and negative external isotropic pressure. This allows for anisotropic unit-cell relaxation, which is important for other phases than the cubic.

As seen in Fig. 2, the energy differences associated with structures of different symmetry and coordination are rather small, so this constitutes a rather sensitive test of a pseudopotential. Table I reveals that our pseudopotential *(A)* agrees very well with available experimental data for the (*t*-*m*)

TABLE I. Adiabatic structural energy differences (eV/ZrO_2) for low-pressure ZrO_2 phases. Pseudopotential (*A* and *C*) calculations were performed with the same calculational parameters.

Energy difference	Pseudopotential *A*	Pseudopotential *C*	Experiment	All-electron FLAPW
Tetragonal-monoclinic	0.077	−0.050	0.06[a]	
Cubic-tetragonal	0.031	0	>0	0.009[b]

[a]Reference 54.
[b]Reference 21.

TABLE II. Electronic valence charge distribution for bulk t-ZrO_2 around ionic sites.

Ionic site	Pseudopotential set A	B	C	All-electron FLAPW
Zr	1.01	1.02	1.04	1.18[a]
O	5.47	5.44	5.47	5.47[a]

[a]Reference 54.

structural energy difference. Considering the smallness of the (c-t) structural energy difference, the agreement with an all-electron full potential linear augmented plane-wave (FLAPW) study[21] is also satisfactory. In this table, it is also clear that pseudopotential *(C)* fails to predict the proper structural ordering; we will comment further on this below. We have not attempted to compare in detail with experiments at elevated temperatures, since it is necessary then to consider the free energy, which we have not calculated here.

We have also plotted the experimentally determined volumes in Fig. 2 for comparison, shown as arrows. The values we have found in the literature display a scattering of order 1%, reflecting a sensitivity on sample preparation and experimental procedure. We have extrapolated high and room temperature data to $T=0$ using the measured thermal expansion coefficient[55] $\gamma=12\times10^{-6}$ K^{-1} for t-ZrO_2. For m-ZrO_2 we have used the value[54] $\gamma=1\times10^{-6}$ K^{-1}, which we have also applied to extrapolate the lattice constants of the cotunnite phase (*Pnam* symmetry), since γ has not been reported for this phase to our knowledge. c-ZrO_2 is unstable at low temperature — the $c\rightarrow t$ transition is a barrierless transformation. Thus the assignment of a $T=0$ volume for c-ZrO_2 is associated with some uncertainty since it involves extrapolation of very high temperature data or finite stabilizer concentration data. Data extrapolation of the latter[56] indicates that the volume difference between c-ZrO_2 and t-ZrO_2 is less than 1%, which is within the overall scattering of the experimental data. Therefore we have not plotted an experimental volume for c-ZrO_2.

Our pseudopotential reproduces experimental volumes to within 1%, which falls within the confidence level of the LDA itself. In other words, the errors induced by the pseudopotential approximation are smaller or comparable to the errors inherent in the LDA. Also, the internal fractional coordinates generally agree well with those reported from x-ray analysis, although the tetragonal oxygen distortion coordinate $d_z=0.033$ is somewhat underestimated compared to the experimental value $d_z=0.065$ measured at 1523 K.[33] However our value of d_z compares very well with the value $d_z=0.029$ obtained by FLAPW calculations[21] and the discrepancy with experiment is mainly traced to thermal volume expansion, since the t-distortion d_z increases with volume, as discussed in Ref. 21.

Table II displays calculated net ionic charges in bulk t-ZrO_2 as a function of pseudopotential and compares to the all-electron FLAPW predictions. The ionic charges were obtained by integrating the valence charge inside spheres around O and Zr sites of radius 0.894 and 1.058 Å, respectively. The unit cell dimensions are $a=5.149$ Å and $c=5.271$ Å and the oxygen t distortion $d_z=\Delta z/c=0.065$. The charges for pseudopotentials *(A)* and *(C)* were obtained at 800 eV, and at 1200 eV for pseudopotential (B); otherwise the same calculational parameters were employed, as described above. The charges here differ from that expected from the nominal ionic charges due to their dependence on the integration sphere radii. The integration spheres, which are not space filling, as well as a, c, and d_z are chosen for direct comparison with the FLAPW results.

We obtain ionic charge transfer in reasonable agreement with the all-electron FLAPW study above and the changes in charge transfer are marginal if we substitute our soft oxygen pseudopotential *(A)* with the harder pseudopotential *(B)*. The charge transfer is also well described by pseudopotential *(C)* even though it fails to predict the structural energies properly, as we now describe.

The calculations using pseudopotential set *(A)* and *(C)* were performed using same calculational parameters (kinetic energy cutoff, k-point sampling, etc.). It is seen in Table I that pseudopotential *(C)* fails to predict m-ZrO_2 as the ground state and that the t distortion vanishes; the c-ZrO_2 phase is overstabilized by pseudopotential *(C)*. Thus, even though the important property of charge transfer is correctly modeled by pseudopotential *(C)*, other aspects of bulk atomic and electronic structure are poorly represented by pseudopotential *(C)*.

Today a variety of techniques for generating smooth, norm conserving pseudopotentials exists.[57,58,42,52] A pseudopotential corresponding to a given atomic species generally looks quite different, depending on the applied pseudopotential generation scheme. These differences reflect the fact that norm conservation does not uniquely determine a pseudopotential and other auxiliary conditions must be imposed. The failure of pseudopotential *(C)*, which was generated using smaller cutoff radii than pseudopotential *(A)*, clearly demonstrates that transferability is sensitive to the choice of these auxiliary conditions and more research is needed into devising optimal auxiliary conditions for pseudopotential generation. It still remains a standard task of a theoretical study to demonstrate the transferability of the pseudopotentials applied.

III. SURFACE GEOMETRIES

The excellent representation of bulk properties by our pseudopotential gives us confidence to employ it in surface calculations, which we now discuss. Predicting the most stable surface structure corresponding to a given set of Miller indices is a very difficult problem in general. The celebrated Takayanagi reconstruction[59] of the Si(111) surface is probably the best example of this. The purpose of our work is to determine the surface energies of the as-cleaved crystals and the local relaxations of these surfaces. Thus we do not consider complex, extended reconstructions. Nor do we consider nonstoichiometric surfaces, that is, our calculational unit cells consist of an integer number of ZrO_2 formula units.

A. Cutting a perfect crystal

Unlike simple homogeneous crystals, in the case of zirconia it is not straightforward to identify the structure of the stable surfaces corresponding to a given Miller plane, due to the chemical and structural complexity. However, the num-

ber of candidates may be winnowed down by adopting a few simple, intuitively plausible rules:

(i) Surface compactness: the most stable surface for metals is usually the most compact one and on a macroscopic scale, the surface energy scales with surface area. For metal oxides, it is also natural to expect the more stable surfaces to be compact to some extent (compactness condition).

(ii) The ion coordination loss by creating the surface should be minimized. Since the cutting surface may be translated arbitrarily perpendicular to the desired Miller plane, it is possible to accomplish this goal. This criterion is not as important for ionic materials as for covalent materials, due to the long-ranged nature of the Coulomb forces, but it is a good auxiliary criterion due to the partial covalency that is always present (bond-breaking condition).

(iii) Avoid polar surfaces: these are notoriously metastable, due to long-ranged electrostatic forces. Generally speaking, the electrostatic interaction energy due to the surface may be lowered by identifying blocks in the perfect crystal with vanishing low-order multipole moments and then forming the surface using these blocks. However, the size of a block increases as the required number of vanishing low-order multipole moments increases and a conflict with the above compactness criterion (i) arises. The resulting balance will be determined by the structure and symmetry of the underlying crystalline structure. An example of this building block principle is the octopolar reconstruction on NiO(111) (Ref. 60) (electrostatic condition).

We have applied the slab technique in our study of ZrO_2 surfaces. We have chosen the slab such that the surfaces on each side of the slab are equivalent and are related by an inversion or mirror/glide type symmetry operation located in the middle of the slab. This has been possible in all cases, due to the particular space groups of *c*-, *t*-, and *m*-ZrO_2.

We have relied on the simple rules outlined above when producing a guess on the atomic structure of the most stable unrelaxed surface corresponding to a given set of Miller indices. In Figs. 6–10 we have shown the upper half of the computational unit cell corresponding to each inequivalent surface. The lower halves of the slab unit cells are mirror/inversion images of the displayed upper halves. All our initial slab structures have been set up so that they have no net dipole moment. This is not obvious to the eye, but in Secs. IV D 1 and IV D 2 we will comment in more detail on the layering structure. In some cases, however, the simple rules outlined above lead to multiple (apparently equally good) guesses on low-energy cleaving and in such cases we have tested several possible terminations.

B. Slab geometry and computational parameters

It is important to check that the thickness of the slab and pseudovacuum are sufficient that finite-size effects do not affect the surface properties and that surface properties are well converged with respect to computational parameters as well.

When studying surface relaxations, two different sets of length scales determine the convergence of surface properties:

(1) The perturbation on the electronic structure caused by the surface must have decayed going from one side of a slab to the other so that the surfaces do not interact with each other. This length scale is usually manageably short, typically a few atomic layers, for ionic materials, which have a significant band gap. For MgO(001), the surface energy has been found to be converged using 4 layers, corresponding to a slab thickness of 4 Å.[47] At the other extreme, *s*,*p* metals exhibit length scales that are considerably longer.

TABLE III. Convergence with respect to calculational parameters for the unrelaxed $t(001)$ surface of ZrO_2. E_{cut} is the kinetic energy cutoff in the plane-wave expansion.

Layers of ZrO_2	Layers of Vacuum	E_{cut} (eV)	Pseudopotential set	*k* points in SBZ	Surface energy (mJ/m^2)
4	4	700	*A*	5	1961
6	4	700	*A*	5	1948
4	6	700	*A*	5	1948
4	4	700	*A*	8	1983
4	4	1000	*A*	5	1961
4	4	1000	*B*	5	1964

(2) The surfaces on each side of the slab may interact through long-range strain fields induced by ionic relaxations. The magnitude of this effect is rather dependent on surface orientation and the material; for metals, the interlayer relaxations typically fall below the experimental thresholds after 3–4 layers (~5 Å).[61] For ZrO_2, our results and those of Orlando *et al.*[19] indicate a comparable average length scale for the depth of the ionic relaxation. For TiO_2, Bates *et al.*[62] find that the surface relaxations have converged, when the slab thickness exceeds 4–5 layers. Of course, the electronic structure and ionic relaxation length scales become indirectly coupled.

In Table III, we have checked the influence of varying slab thickness as well as other computational parameters for the unrelaxed $t(001)$ surface shown in Fig. 6 to address point (1) above. It appears that the electronic structure of the slab surfaces are sufficiently well converged using a slab and pseudovacuum thickness of 4 layers each, corresponding to 10 Å each. Furthermore, a kinetic energy cutoff at 700 eV and a 5 *k*-point sampling in the surface Brillouin zone (SBZ) gives well converged surface energies. 5 *k* points in the SBZ corresponds to a sampling spacing of 0.10 $Å^{-1}$. This relatively large sampling spacing is sufficient because no surface metallization occurs. We have checked this for all surfaces of *c*-ZrO_2, which are the most likely to exhibit metallic behavior. Bulk *c*-ZrO_2 has a smaller band gap in the eigenvalue spectrum than bulk *t*-ZrO_2 and *m*-ZrO_2, which has the largest band gap (this band-gap ordering is also found by Hartree-Fock calculations[25] and another LDA study[63] of bulk zirconia). We find that going significantly below 700 eV in kinetic energy cutoff using our pseudopotential leads to inaccurate surface energies.

It is also seen in Table III that the pseudopotentials applied in this study give surface energies in excellent agreement with pseudopotential set (*B*) where the oxygen pseudopotential generated with a more conservative choice of cutoff radii, $r_s = 0.69$ Å and $r_p = 0.69$ Å, discussed in Sec. II B.

To address point (2) above, we increased the slab thickness from 4 to 6 layers for the $t(001)$ surface and relaxed the slab ions. This increased the relaxation energy by 7% compared to the 4-layer slab. Surface bond lengths change less

than 0.004 Å, corresponding to 6% of the bond length relaxation. Finite slab thickness thus accounts for the largest error bar in our predicted relaxation energies. However, since the relaxation energy only gives a minor contribution to the surface energy, typically 25%, this small uncertainty in the results does not affect any of our conclusions. We also notice *en passant* that the relaxation energy does not necessarily increase monotonically with slab thickness; for example, increasing the $m(011)$ slab from 4 layers (7.4 Å) to 6 layers (11.1 Å) actually decreases the relaxation energy by 9%. The upper half of the 6-layer $m(011)$ slab is shown in Fig. 9.

All slab calculations presented in the following are performed with a slab and pseudovacuum thickness of approximately 10 Å each, a plane-wave cutoff of 700 eV, and a k-point sampling spacing of 0.10 $Å^{-1}$.

IV. RESULTS

We now discuss the properties we have calculated for seventeen different surfaces of ZrO_2. In Fig. 1 we have shown full subsets of all principal directions, which are inequivalent by symmetry. For the *c* phase, there are three inequivalent principal directions, five for the *t* phase and nine for the *m* phase. If the point group operators of the space group corresponding to each bulk structure are applied to the subsets shown in Fig. 1, the full set of 26 principal directions is generated for each phase.

For comparison, we have referenced the crystalline directions in the tetragonal structure to the fluorite unit cell in Fig. 1, with the *t* distortion and 4_2 axes in the [001] direction. The monoclinic unit cell has the 2_1 axes along the [010] direction.

A. Surface energetics

In Table IV we show the calculated surface energies for all inequivalent surfaces of the *c*, *t*, and *m* phases, before and after local relaxations of the surface ions. The rms displacement given in Table IV is the average for all N atoms in each slab, corrected for displacement of the geometrical center of mass $\Delta\mathbf{r}_{\mathrm{c.m.}}$, i.e.,

$$\Delta r_{\mathrm{rms}} = \sqrt{\frac{1}{N}\sum_{i=1}^{N} (\Delta\mathbf{r}_i - \Delta\mathbf{r}_{\mathrm{c.m.}})^2}. \qquad (1)$$

This quantity will tend to decrease with increasing slab thickness, since bulk ions have small or vanishing displacement upon relaxation. However, comparison is meaningful because we have chosen all slabs to have approximately the same thickness, ~10 Å, consistent with the layer spacing in each direction.

The unrelaxed slab structures have been ''carved'' out of the respective bulk crystal according to the simple principles outlined in Sec. III A, where the bulk crystal structures have been relaxed fully with respect to intracell and unit cell degrees of freedom, corresponding to the minima in Fig. 2. All atoms in our slab calculations have been allowed to relax, but the surfaces on both sides of the slab stay equivalent by a symmetry operator, inversion, or a mirror/glide plane, located in the middle of the slab. The symmetry operator in the middle of the slab in each case is also present in the parent crystal from which the slab has been cut. The slab unit cell has not been allowed to relax — it is considered pinned to the equilibrium bulk size, shape, and orientation corresponding to the minima in Fig. 2. This is a stabilizing factor for the tetragonal slab structures, opposing a possible transition to local monoclinic coordination, which is favored at low temperatures. However, since the *c*-*t* phase transition is a barrierless intracell distortion, *c*-ZrO_2 will always distort to *t*-ZrO_2 on relaxing ions (even without unit cell relaxation) and thus the relaxation energy is not a surface confined quantity, but scales with the bulk size. Therefore we do not report relaxation energies for the *c*-ZrO_2 surfaces.

TABLE IV. Surface energies for principal ZrO_2 phases at $T = 0$ K. A * symbol indicates that structure transforms from cubic to tetragonal. The transformation energy is proportional to the slab thickness and therefore the relaxed surface energy is not well defined in these cases.

Face		Surface energy (mJ/m^2)		% Relaxation energy	rms ionic relaxation (Å)
		Unrelaxed	Relaxed		
Cubic	(100)	3058	*	*	*
	(110)	2288	*	*	*
	(111)	1193	*	*	*
Tetragonal	(001)	1961	1577	20 %	0.11
	(100)	3286	1684	49 %	0.28
	(110)	2327	1532	34 %	0.41
	(101)	2322	1694	27 %	0.13
	(111)	1315	1239	6 %	0.06
Monoclinic	(001)	2432	1804	26 %	0.31
	(010)	3504	2464	30 %	0.15
	(100)	2283	1833	20 %	0.12
	(110)	2249	1642	27 %	0.15
	(101)	2729	1968	28 %	0.31
	($0\bar{1}1$)	2307	1730	25 %	0.13
	($\bar{1}01$)	2022	1512	25 %	0.25
	($1\bar{1}1$)	1862	1537	17 %	0.13
	($\bar{1}11$)	1602	1246	22 %	0.09

From Table IV we see that the (111) and ($\bar{1}11$) faces are the most stable stoichiometric surfaces of the *t* and *m* phases, respectively, and also that the surface energy is considerably anisotropic. For both phases, the surface energy difference between the most stable and second most stable surface is considerably larger than the intrinsic uncertainty in the relaxation energy discussed in Sec. III B.

Examination of Table IV reveals that there is a natural correlation between low unrelaxed surface energies and low rms ionic relaxations, Eq. (1). Basically, surfaces that are relatively stable to begin with do not relax much further. There is an even stronger correlation between the unrelaxed surface energy and the magnitude of the surface energy relaxation; this is shown in Fig. 3. The latter is an expression of the fact that there is some lower bound $E_{s,\mathrm{min}}$ on the surface energy and only some fraction α of the difference between the lower bound and unrelaxed surface energy $E_{s,\mathrm{unr}}$ may be regained by local bond rearrangement at the surface, leading to the relaxed surface energy $E_{s,\mathrm{rlx}}$. We have shown

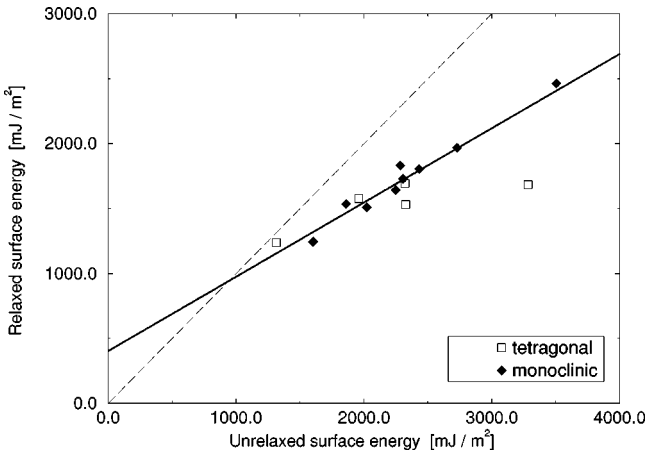

FIG. 3. Relaxed and unrelaxed surface energies calculated for tetragonal and monoclinic zirconia at $T=0$. The solid line corresponds to linear regression through all data points. The intersection with the dashed line ($E_{s,\mathrm{rlx}}=E_{s,\mathrm{unr}}$) corresponds to $E_{s,\mathrm{min}}$.

a regression analysis on this simple scaling hypothesis

$$\alpha=\frac{E_{s,\mathrm{rlx}}-E_{s,\mathrm{min}}}{E_{s,\mathrm{unr}}-E_{s,\mathrm{min}}} \tag{2}$$

in Fig. 3. The regression analysis gives the values $\alpha=0.57$ and $E_{s,\mathrm{min}}=942\ \mathrm{mJ/m^2}$ as parameters characterizing the material ZrO_2. The same scaling seems to apply to the low index surfaces of both *t* and *m* phases, as judged from the limited data set available. One point of the tetragonal data set, corresponding to the $t(100)$ surface, seems to deviate significantly from the trend; we will comment on this later in Sec. IV D 1.

The surface energy of the most stable monoclinic and tetragonal relaxed surfaces are equal, to within the calculational accuracy. One would also expect this on the basis of the empirical observation that surface energy scales roughly with the cohesive energy, for a given type of bonding. Since

$$\frac{\Delta E^{\mathrm{coh}}(t-m)}{E^{\mathrm{coh}}(m)}<1\%, \tag{3}$$

then particular details of the surface geometry and electronic structure will determine which phase has the most stable termination.

To our knowledge no surface energy measurements for pure, crystalline ZrO_2 have been reported. However, for polycrystalline ZrO_2 containing 6% CaO, Sotiropoulou and Nikolopoulos[30] used the multiphase equilibration technique for the measurement of contact angles at high temperatures and extrapolated a surface tension of $1428\ \mathrm{mJ/m^2}$ at 0 K. Likewise, for polycrystalline ZrO_2 containing 8% Y_2O_3, Tsoga and Nikolopoulos[31] extrapolated high-temperature data to get a surface tension of $1927\ \mathrm{mJ/m^2}$ at 0 K. It is well known that such measurements are both difficult and subject to large error bars.[27] However, it is still satisfying to see that our calculated surface energies are consistent with available experimental results. Our result for $t(001)$is also in good agreement with a Hartree-Fock slab calculation,[19] which gave $1850\ \mathrm{mJ/m^2}$ for the unrelaxed surface and $1630\ \mathrm{mJ/m^2}$ for the relaxed $t(001)$ surface. Due to the computational demanding nature of these calculations, these authors were only able to obtain results for a three-layer slab, whereas our $t(001)$ slab has four layers.

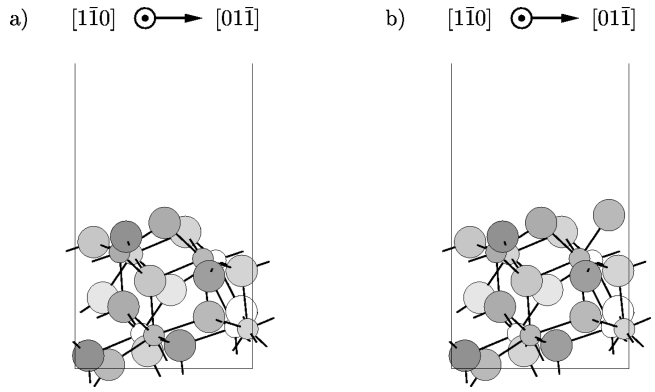

FIG. 4. (a) The $m(111)$ termination used in our study. (b) The $m(111)$ termination proposed by Cerrato *et al.* (Ref. 15). The figure shows the two topmost layers and in both cases the structures are unrelaxed. Zr ions are small and O ions are large. Ions in the foreground are shaded darker than ions in the background.

In the literature, it is still an open question whether the GGA gives an improved surface description compared to the LDA. There seems to be a consensus that the GGA improves the description of atoms and molecules, but for bulk systems a tendency to overcorrect the LDA has been reported.[28] The LDA predicts surface energies for metallic surfaces in good agreement with experimental data.[36,37] We do not report surface energies using the GGA for the ZrO_2 surfaces, because our pseudopotentials presented in Sec. II A have been generated using the LDA. Formally, this makes application of the GGA physically unclear using these pseudopotentials for the ion-electron interaction. However, we tested the GGA for a few ZrO_2 surfaces using our LDA pseudopotentials and found a consistent drop in the surface energy of order 10–15 %. A drop in surface energy by applying the GGA has also been observed for the $TiO_2(110)$ and $SnO_2(110)$ surfaces.[29,62] Comparison of Table IV with the available experimental data mentioned above does not indicate a systematic overestimation of the surface energies for ZrO_2. Thus, consistent inclusion of the GGA is unlikely to affect our conclusions about which surfaces are most stable. Also, for the ZrO_2 surfaces where we tested the GGA, the ionic relaxations changed rather insignificantly (the rms ionic relaxation changed no more than 0.01 Å).

For *t*-ZrO_2 Morterra *et al.*[12,13] using Fourier-transform infrared spectroscopy (FTIR) and high-resolution transmission electron spectroscopy (HRTEM) found that $t(111)$ was the most abundant termination in sintered *t*-ZrO_2 powders, which is in agreement with our surface energy calculations. This result is consistent with results for other oxides with fluorite type structures,[64] e.g., UO_2, which has the (111) face as its most stable surface.

Recently, on the basis of XRD, FTIR, and HRTEM measurements on *m*-ZrO_2 powders, Cerrato *et al.*[15] concluded that the $m(111)$ surface was thermodynamically the most stable *m*-ZrO_2 termination. These authors proposed an $m(111)$ termination different from the one we have used in our study. In Fig. 4 we have shown the two possible terminations side by side. One can see that the alternative termi-

nation in Fig. 4(b) proposed by Cerrato *et al.* is nonstoichiometric (it has one excess O ion per surface unit cell), which implies that this structure is not electrostatically stable due to the ionic nature of ZrO_2, as also noted by Cerrato *et al.*

These authors reason that dissociative adsorption of H_2O may electrostatically stabilize the surface at lower temperature, but they do not discuss a mechanism of stabilization in the high-temperature regime, where the OH groups and physisorbed H_2O molecules are desorbed.

The additional O ion in the structure proposed by Cerrato *et al.* must be rather loosely bound, since it only coordinates to a single, sevenfold coordinated Zr atom, as seen in Fig. 4(b). We want to point out that the FTIR measurements presented by these authors do not unambiguously determine a specific surface structure of the $m(111)$ face, due also to the influence of other faces, edges, and defects present on the particles. Further, kinetic and finite-size effects, due to the long-ranged nature of electrostatic forces, may be important in explaining the experimentally derived surface morphologies.

Another possibility is that concomitant formation of O vacancies and other surface/interior defects at high temperatures might provide a source of oxygen for the formation of such nonstoichiometric surface facets, if the proposed structure indeed corresponds to the experimental data. However, segregating an O ion to the surface by creating a bulk O vacancy is an endothermic process. Therefore it is likely that the structure proposed by Cerrato *et al.*, if correct, is a kinetically stabilized structure achieved by quenching a thermodynamically less stable structure formed at high temperature. At low temperature, then, we do not believe that this can be the most stable structure. We have not considered surface energetics under O-rich conditions in our calculations, due to computational difficulties and ambiguities.

When comparing our results to experimental data obtained at elevated temperatures, typically in the interval 300–1500 K, it is necessary to include the surface entropy. The surface entropy for ZrO_2 is of order $0.4\ \mathrm{mJ/(m^2\ K)}$.[31] Surface entropy differences are then expected to be smaller, properly of order $0.1-0.2\ \mathrm{mJ/(m^2\ K)}$. Therefore most of our conclusions should be qualitatively valid at medium high temperatures as well, i.e., up to 800–1000 K, since we find a surface energy difference $\sim 300\ \mathrm{mJ/m^2}$ between the most stable and second most stable surface for both *t*- and *m*-ZrO_2.

B. Coordination analysis

We have also investigated possible coordination trends in the energetics. First we need to define a measure of interatomic coordination. Due to the structural complexity of ZrO_2 and due to the desire to treat relaxed structures on an equal footing with unrelaxed ones, a continuous definition of coordination is necessary. We define the coordination of atom i as

$$\Gamma_i = \sum_{j \neq i} f\left(\frac{r_{ij}}{\lambda}\right), \tag{4}$$

where j runs over all other atoms and $f(s)$ is a decaying function counting the number of neighbors within a certain characteristic distance λ.

TABLE V. c^{ν}_{loss} for most/least stable t and m surfaces for different values of ν.

surface	ν		
	2	24	∞
$t(100)$	0.288	0.298	0.304
$t(111)$	0.214	0.173	0.176
$m(0\bar{1}0)$	0.238	0.241	0.224
$m(\bar{1}11)$	0.193	0.143	0.135

For $f(s)$ we will use the function family

$$f^{\nu}(s) = \left(\frac{V^{\infty}}{V^{\nu}}\right) e^{-s^{\nu}}, \tag{5}$$

where ν is a form parameter giving the sharpness of the cutoff in $f^{\nu}(s)$ around $s=1$ and V^{ν} is the integral

$$V^{\nu} = 4\pi \int_0^{\infty} t^2 e^{-t^{\nu}} dt. \tag{6}$$

The limit $\nu=\infty$ corresponds to a sharp cutoff at $s=1$. The normalization in Eq. (5) makes Γ_i independent of ν for a continuous distribution of atoms.

We also define the specific (per unit area) coordination loss for a surface structure as

$$c^{\nu}_{\mathrm{loss}} = \frac{N\gamma^{\nu}_{\mathrm{bulk}} - \Gamma^{\nu}}{A}, \tag{7}$$

where A is the total slab surface area per unit cell, N the number of formula units per unit cell, $\Gamma^{\nu} = \Sigma_{i=1}^{3N} \Gamma_i^{\nu}$, and $\gamma^{\nu}_{\mathrm{bulk}}$ the average coordination per formula unit in the corresponding bulk. Loosely speaking, c^{ν}_{loss} counts the number of cut ''bonds'' at the surface per unit area.

We set $\lambda = 2.432$ Å, which is between the first and second coordination shell for both *m*- and *t*-ZrO_2. We use $\nu=24$, which discriminates the farthest first neighbor from the closest second neighbor by a factor of 9 in the weight function in Eq. (5). We notice that although the absolute value of c^{ν}_{loss} defined above is sensitive to the choice of ν, trends in c^{ν}_{loss} are less sensitive. This is demonstrated in Table V.

In Fig. 5 we have shown the correlation between surface energies and coordination, as defined in Eq. (7). One notices a natural correlation between openness of the surface and surface energy. The correlation is more irregular than for metallic systems, where the surface energy to a good approximation is a simple nonlinear function of surface coordination loss.

It is seen that *m* surfaces generally are more sensitive to coordination loss than *t* surfaces [Figs. 5(a) and 5(b)]; this is to be expected to some extent, since the *m* phase Zr is sevenfold coordinated whereas the *t* phase Zr is eightfold coordinated — therefore it is more expensive for a *m* Zr atom to lose a neighbor than a *t* Zr atom. Notice that often the coordination *decreases* upon relaxing the surface ions [Fig. 5(c), where often $\Delta c_{\mathrm{loss}} < 0$], although low coordination still constitutes a driving force for ionic relaxation, as seen from Fig. 5(d). This observation is independent of ν. In most cases the coordination change upon relaxation is rather small as indi-

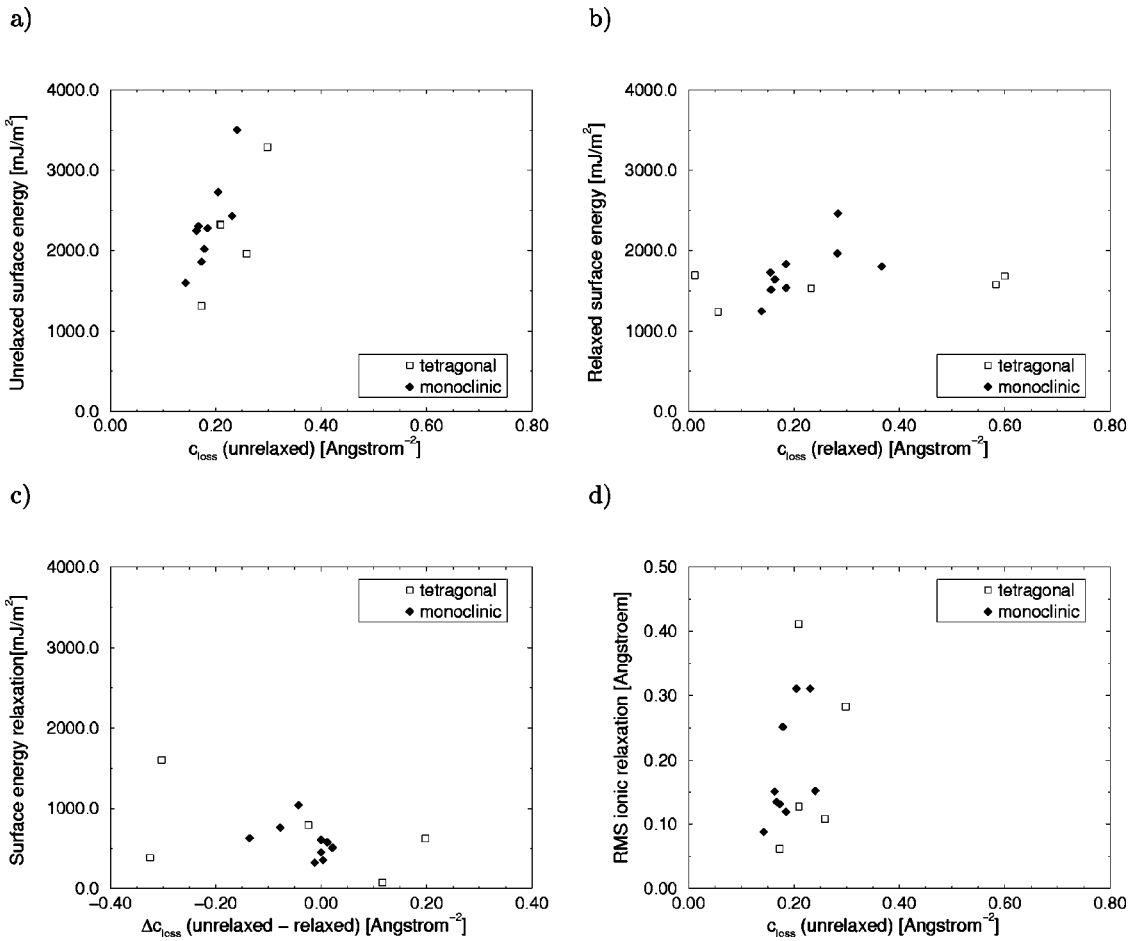

FIG. 5. (a),(b) Correlation between coordination loss, c_{loss}^{ν} [Eq. (7)], and surface energy of unrelaxed and relaxed ZrO_2 surfaces. (c) Correlation between change in coordination loss upon relaxation of surface ions and change in surface energy. (d) Correlation between coordination loss of unrelaxed ZrO_2 surfaces and rms ionic relaxation. In (a)–(d) $\nu=24$ has been used in Eq. (5).

cated by the cluster of points around $\Delta c_{\mathrm{loss}}=0$ in Fig. 5(c). This indicates orientational relaxation is most important for ZrO_2, especially for *m* surfaces. This is consistent with a rigid ion picture of ZrO_2, where bond lengths do not change upon relaxation.

C. Relation to the (*m*-*t*) Martensitic transition

Our results provide some insight into transformations of small particles of zirconia, where the surface energy is comparable to the bulk phase transformation energy. It is well known that small zirconia particles suspended in a host matrix do not transform from tetragonal to monoclinic, even well below the bulk transition temperature unless subjected to an external stress field, such as in the vicinity of a propagating crack. Since the specific volume of the *m* phase is 4% larger than the *t* phase this transition opposes the propagation of the crack. This mechanism is known as transformation toughening.[65] However, the lowering of the $(t\rightarrow m)$ transition temperature is also observed in small free ZrO_2 particles.[66] It has been conjectured that this intrinsic size effect is driven by a larger surface tension for the *m* phase than the *t* phase. This is at variance with our results in Table IV, suggesting that the surface tensions of the most stable *t* and *m* faces are approximately equal. However, a closer look at our results may reconcile this apparent contradiction.

It is well established that a definite orientation relationship exists between crystalline directions upon the $(t\rightarrow m)$ transition.[67,68] It is found that $(100)_m\|(100)_t$ and $[001]_m\|[001]_t$ ($T<1000$ °C), $[010]_m\|[001]_t$ ($T>1000$ °C). By the Wulff construction, one expects the $t\{111\}$ facets to dominate in small *t* crystallites. Due to the orientation relationship above, upon the $(t\rightarrow m)$ Martensitic transition we obtain

$$t\{111\}\rightarrow\begin{cases} m\{\bar{1}11\} \\ m\{111\} \end{cases} \tag{8}$$

in equal amounts. As seen in Table IV, the $m\{\bar{1}11\}$ faces have the same stability as $t\{111\}$ faces, whereas the $m\{111\}$ are less stable. To summarize our point, *the orientational constraint on the (t→m) Martensitic transition forces favorable t surfaces to turn into unfavorable m surfaces, which inhibits the transformation.*

A small additional contribution to increasing the monoclinic surface energy per particle of course also comes from the volume expansion of 4% upon the $(t\rightarrow m)$ transition. Furthermore, a complete understanding of the transition temperature depression necessarily also involves other finite size effects, such as edge effects. The net result is that the surface of an *m*-phase particle would appear to have a larger surface energy than a *t*-phase particle. Due to the R^3 scaling of the

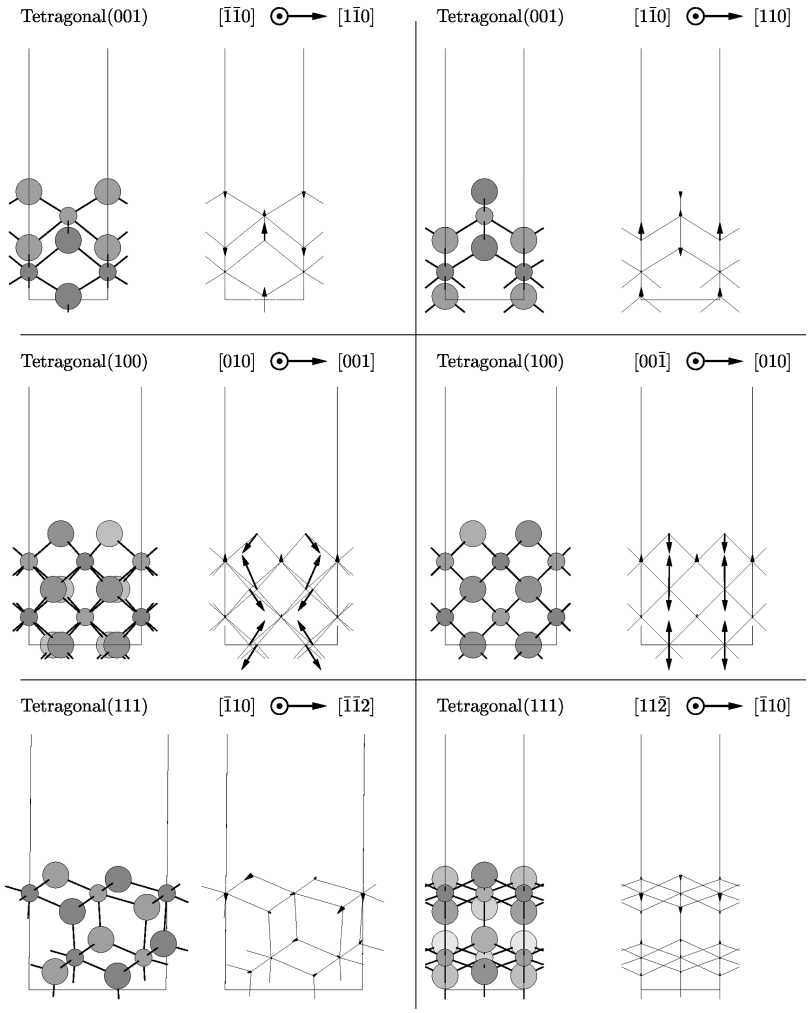

FIG. 6. $t(001)$, $t(100)$, and $t(111)$ ZrO_2 surfaces, viewed from two angles. Corresponding crystal directions are shown at the upper right of each panel. Left side in each box: the (upper half) unrelaxed slab unit cell. Right side in each box: arrows indicate direction and $4\times$ magnitude of ionic relaxations, corresponding to the slab on the left side in each box. Zr ions are small and O ions are large. Ions in the foreground are shaded darker than ions in the background.

$(m\text{-}t)$ bulk transition energy and the R^2 scaling of the surface energy, where R is the particle radius, this implies a critical particle radius R_c, below which the particle does not undergo the $(t\rightarrow m)$ transition at all. For a qualitative estimate of R_c, it is necessary to include the entropy of bulk and surface t- and m-ZrO_2, which we have not tried to calculate. Using x-ray diffraction (XRD), R_c is experimentally believed to be in the vicinity of 150 Å.[66,15]

Our conclusion must be considered tentative with respect to embedded ZrO_2 particles, because the surface energy is of course different from interfacial energies and interface mismatch factors may be different for different ZrO_2 phases. However, according to Miedema's semiempirical rules,[69] one expects the mismatch energy for large angle grain boundaries to scale with the respective surface energies and the interface bond energy to be independent of bulk structure.

D. Surface structures

In this section we show pictures of the unrelaxed surfaces of ZrO_2 as well the magnitude of the relaxations of the surface ions and we discuss the particularly interesting features of each surface. In order to avoid pictures that are too cluttered, we have shown only the symmetry inequivalent atoms in each slab unit cell, i.e., only the atoms between the middle of the slab and one of the slab surfaces.

1. Tetragonal surfaces

In Figs. 6 and 7 we have shown the unit cells of the five unrelaxed t-ZrO_2 surfaces and the ionic relaxations, indicated by magnified arrows. We have referenced all crystalline directions to the CaF_2 unit cell, shown in Fig. 1(a).

The c and $t(001)$ surfaces are characterized by alternating columns of O atoms perpendicular to the surface; half of the columns (t columns) have a terminating O atom above the outermost Zr layer and these O atoms terminate the surface. The other half of the O columns (s columns) are terminated below the outermost Zr layer. For the unrelaxed $t(001)$ surface, the t distortion is perpendicular to the surface, so that the t columns are displaced inwards, whereas the s columns are displaced outwards compared to the $c(001)$ surface. This corresponds to a flattening of the $c(001)$ surface. The other possibility, corresponding to a roughening of the $c(001)$ surface, so that the t columns and s columns are displaced out-

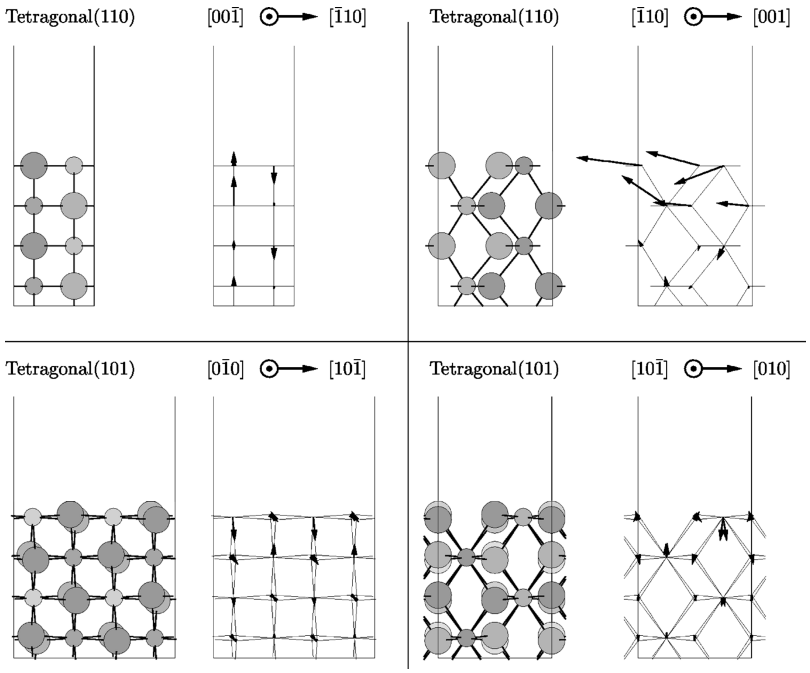

FIG. 7. $t(110)$ and $t(101)$ ZrO_2 surfaces, viewed from two angles. Corresponding crystal directions are shown at upper right of each panel. Left side in each box: the (upper half) unrelaxed slab unit cell. Right side in each box: arrows indicate direction and 4 × magnitude of ionic relaxations, corresponding to the slab on the left side in each box. Zr ions are small and O ions are large. Ions in the foreground are shaded darker than ions in the background.

wards and inwards, respectively, have significantly higher surface energy. This is consistent with the fact that the *t* columns relax further inwards, when the ions are allowed to relax on the $t(001)$ surface, whereas the *s* columns are displaced correspondingly outwards. Thus the $t(001)$ surface is flattened further on relaxation.

For the $t(100)$ surface, the *t* distortion is parallel to the surface. The ionic relaxations are far more significant at this surface. A closer view of the relaxed $t(100)$ surface shows that the *t* distortion has been rotated to be perpendicular to the surface. This is an interesting result, because it indicates that the surface determines the direction of the *t* distortion in the bulk. The barrier for this transition is probably rather small. A preferential direction for the *t* distortion is only seen for $t(001)$ and $t(100)$ and is properly related to the fact that these surfaces must be partially O terminated in order to be nonpolar. The rotation of the *t* distortion, which also affects the interior of the slab significantly, is the reason why the $t(100)$ surface deviates from the trend in Fig. 3. The relaxed surface energy of $t(100)$ in Table IV is slightly higher than $t(001)$ due to a small residual unit cell strain; the *t* distortion is accompanied by a small unit cell elongation and this effect is not picked up when the slab unit cells are held fixed.

The remaining *t*-ZrO_2 surfaces have a more homogeneous layer structure, the layers being charge neutral, as seen in Figs. 6 and 7. The $t(110)$ and $t(101)$ differ only in the orientation of the *t* distortion with respect to the surface (this results in different sizes of minimal slab unit cells). Both surfaces undergo the same type of characteristic rumpling distortion, where the topmost Zr atoms relax inwards, the surface O atoms and second layer Zr atoms relax outwards. The $t(110)$ surface is seen to have the largest distortions of all the surfaces, but they are primarily confined to the two topmost atomic layers. Note that these distortions, though they are the largest of any surface studied, are not as effective in reducing the surface energy as in the $t(100)$ surface (see Table IV). The most stable *t* surface, $t(111)$, is compact and the ionic relaxations are small and confined to the topmost layer.

2. Monoclinic surfaces

In Figs. 8, 9, and 10 we have shown all the *m* surfaces as well as the ionic relaxations, indicated by magnified arrows. We have referenced all crystalline directions to the conventional unit cell with [010] as the unique direction, as shown in Fig. 1(c).

As for *t*-ZrO_2, the most stable surface $m(\bar{1}11)$ is compact, with small relaxations confined to the topmost layer. The least stable principal surface, $m(010)$, has a rather corrugated appearance.

The *m* surfaces are more complex than the *t* surfaces and therefore more difficult to rationalize and compare. Therefore we find it instructive to discuss the layering structure in more detail to elucidate similarities and differences. First one has to clarify the meaning of a crystal plane. We define a *plane* as the thinnest possible planar structure parallel to the surface, which has a center of symmetry in the middle and is mapped onto all planes below it by applying symmetry operators (translations, screw axes, or glide planes) — thus a plane has no net dipole moment. All ions must belong to only one plane. This definition means there will be an integer number of planes per *Miller plane*, one or two for the case of *m*-ZrO_2. Each plane has either *single* or *double layer structure*. A single layer is characterized by an almost flat layer of Zr ions in the middle. Double-layer structures are composed by two single layers connected by a symmetry center, so that the net dipole of the double layer vanishes. Single-layer

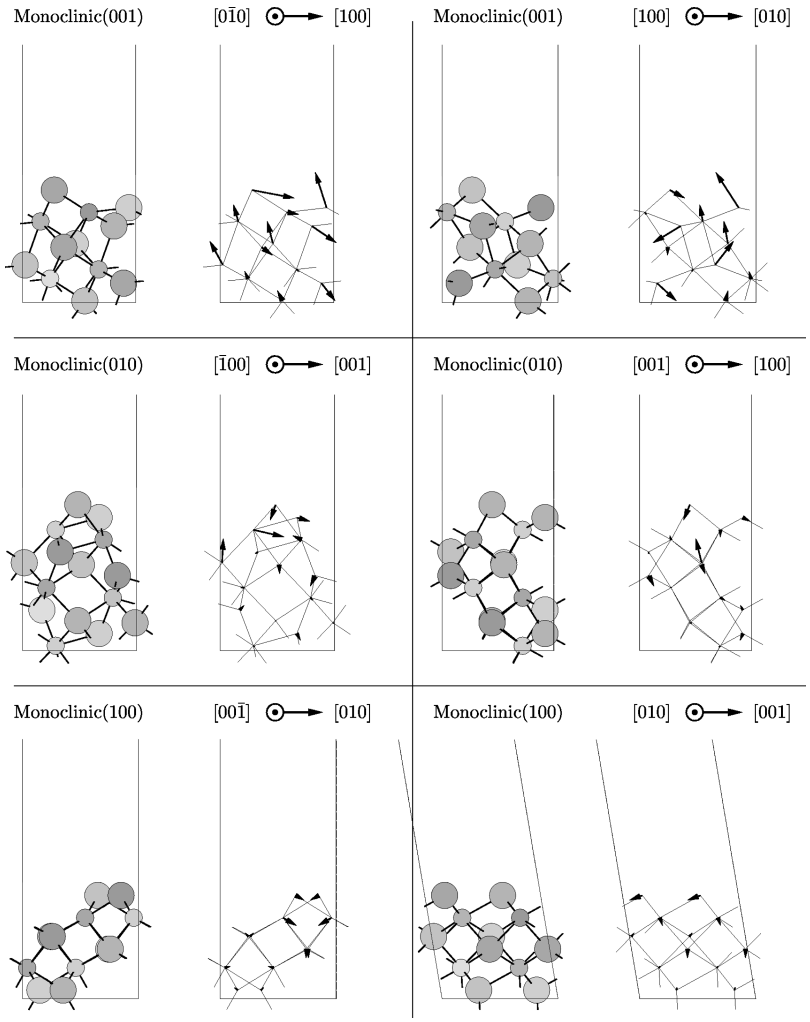

FIG. 8. $m(001)$, $m(010)$, and $m(100)$ ZrO_2 surfaces, viewed from two angles. Corresponding crystal directions are shown at upper right of each panel. Left side in each box: the (upper half) unrelaxed slab unit cell. Right side in each box: arrows indicate direction and 4× magnitude of ionic relaxations, corresponding to the slab on the left side in each box. Zr ions are small and O ions are large. Ions in the foreground are shaded darker than ions in the background.

planes have symmetry centers in the middle of the plane.

The $m(001)$ and $m(100)$ planes are composed of thick double layers and subsequent double layers below the surface are connected by primitive translations. Figure 8 shows one such double layer. $m(010)$, on the other hand, consists of single-layer planes, where two subsequent planes are connected by a 2_1 operation or alternatively a c glide. A plane is connected to the second plane below by a primitive translation. Thus there are two planes per Miller plane. Figure 8 shows the first, second, and half of the third plane.

$m(101)$ and $m(\bar{1}01)$have single-layer plane structures, where two subsequent planes are connected by a 2_1 operation, where the 2_1 axis lies between the single-layer planes, parallel to the surface. Thus there are two planes per Miller plane. Figures 9 and 10 show the three topmost single-layer planes of $m(101)$ and $m(\bar{1}01)$, respectively.

$m(110)$ and $m(011)$ have double-layer-type planes. Figure 9 shows the first and half of the second double-layer plane. $m(111)$ and $m(\bar{1}11)$ have single-layer plane structures, where subsequent planes are connected by primitive translations. Figure 10 shows two single-layer planes for both $m(111)$ and $m(\bar{1}11)$.

We note that much of the large values of rms ionic relaxation for less stable m surfaces in Table IV are due to significant relaxations in the subsurface layers, to a larger extent than the t surfaces.

For the t surfaces, it was found that the $t(100)/t(001)$ as well as the $t(110)/t(101)$ relaxed into similar surface structures. Looking at Table IV, one might suspect that the same was the case for the pairs $m(001)/m(100)$ and $m(110)/m(011)$. A closer inspection of these final structures reveals, however, that although both $m(001)/m(100)$ appear similar, many surface and subsurface atoms have different coordination shells. Likewise, both $m(110)$ and $m(011)$ are rather flat, but some atoms close to the surface have different coordination shells.

It has been stated[39] that for metal oxides, the topmost O ions are generally displaced outwards, whereas topmost cations are displaced inwards. When looking at Figs. 6–10, this rule of thumb does not seem to be particularly well obeyed for ZrO_2 surfaces.

V. SUMMARY

We have studied the surfaces of zirconia (ZrO_2) by first-principles calculations using the local density approximation

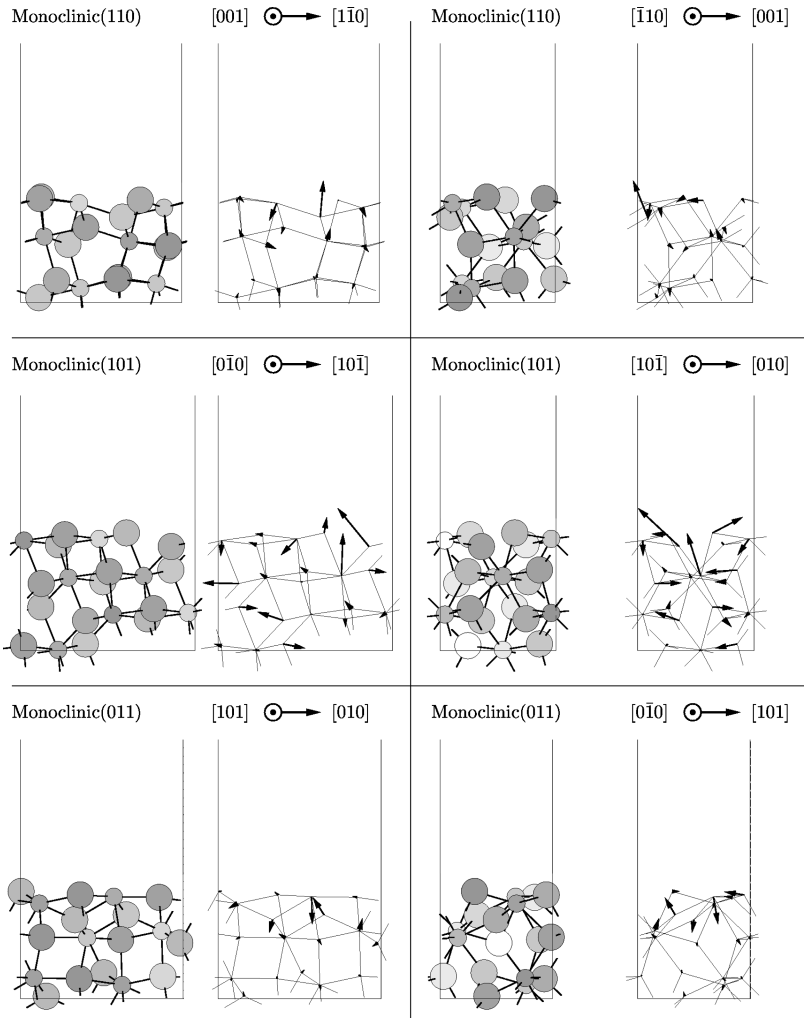

FIG. 9. $m(110)$, $m(101)$, and $m(011)$ ZrO_2 surfaces, viewed from two angles. Corresponding crystal directions are shown at upper right of each panel. Left side in each box: the (upper half) unrelaxed slab unit cell. Right side in each box: arrows indicate direction and 4× magnitude of ionic relaxations, corresponding to the slab on the left side in each box. Zr ions are small and O ions are large. Ions in the foreground are shaded darker than ions in the background.

to density functional theory and the pseudopotential formalism. We have demonstrated that the structural energies of different competing bulk phases of ZrO_2 are well described at this level of theory, lending confidence to our ability to then turn our attention to the surfaces of ZrO_2.

Due to the chemical and structural complexity of ZrO_2 we have focused on stoichiometric, bulk-terminated surfaces determined from simple, intuitively plausible rules. For some surfaces, where the bulk termination is ambiguous, we have considered multiple bulk terminations.

We predicted surface energies and relaxations for the principal surfaces of different bulk phases of zirconia. Our surface energies are in good agreement with available experimental data for stabilizer-doped t-ZrO_2. We find that the stoichiometric (111) and ($\bar{1}$11) faces are the most stable surfaces of the tetragonal and monoclinic phases, respectively, and also that the surface energy is considerably anisotropic.

We find an interesting linear relation between unrelaxed and relaxed surface energies for both tetragonal and monoclinic low index faces of ZrO_2. It remains to be demonstrated whether this relation also applies to nonprincipal and stepped surfaces. Also it would be interesting to investigate whether such a simple scaling behavior is found for other complex oxides as well. On the other hand, we find that the correlation between surface energetics/relaxations and the coordination of surface ions is less compelling.

Our work suggests that the tetragonal(100) surface — if cleavable — will relax into the tetragonal(001), thus rotating the direction of the t distortion below the surface, possibly by a martensitic transformation. We find that the tetragonal (110) and (101) surfaces undergo a rumpling-type distortion. The most stable tetragonal and monoclinic surfaces exhibit a rather small relaxation, confined to the near surface ions. Other surfaces (especially monoclinic), however, display ionic relaxations extending well below the surface. We do not find a clear pattern in the preferred relaxation direction (inwards/outwards) of either Zr or O ions at the surface, contrary to previous suggestions for oxides.

We propose that the surface energy anisotropy is an important key to the detailed understanding of the depression of the tetragonal-monoclinic phase transition temperature in small particles, where surface energetics can dominate bulk stability preferences. Due to the orientational relation between tetragonal and monoclinic phases upon this transition,

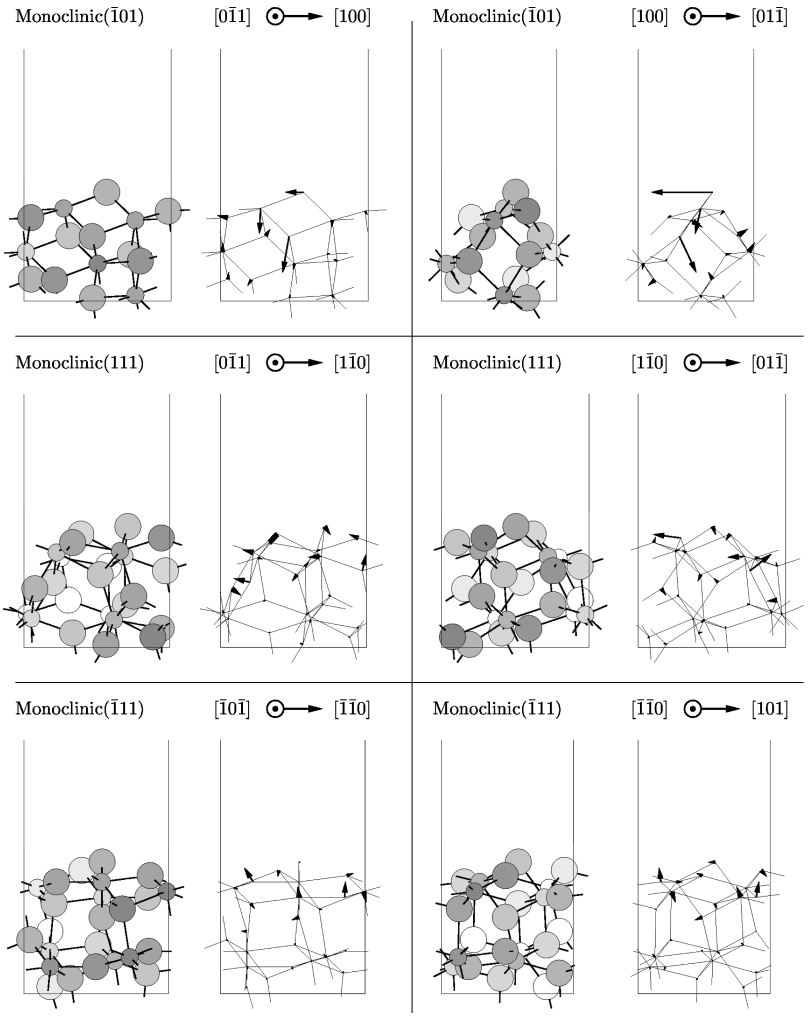

FIG. 10. $m(\overline{1}01)$, $m(111)$, and $m(\overline{1}11)$ ZrO_2 surfaces, viewed from two angles. Corresponding crystal directions are shown at upper right of each panel. Left side in each box: the (upper half) unrelaxed slab unit cell. Right side in each box: arrows indicate direction and 4× magnitude of ionic relaxations, corresponding to the slab on the left side in each box. Zr ions are small and O ions are large. Ions in the foreground are shaded darker than ions in the background.

we propose that stable tetragonal surfaces are forced to transform into less stable monoclinic surfaces, effectively corresponding to a higher surface energy of the monoclinic surfaces, thus lowering the transition temperature.

Suppression of the $t \rightarrow m$ transition is essential for application of t-ZrO_2 as a thermal barrier coating (TBC), since the volume expansion upon the $t \rightarrow m$ transition causes spallation (de-adhesion of the ZrO_2 film coating). It has been recognized for a long time that this might be achieved by preparing the ZrO_2 film coating such that the ZrO_2 crystallites comprising the film remain below a critical radius ~150 Å,[66,15] due to the higher effective surface energy of the monoclinic surface, as found in the present work. On thermal cycling, however, crystallites tend to sinter, eventually to exceed the critical diameter and undergo the $t \rightarrow m$ transition. A major challenge in the future is thus to devise a way to prevent ZrO_2 nanoparticles from sintering upon thermal cycling.

ACKNOWLEDGMENTS

This work was supported by the Air Force Office of Scientific Research (Grant No. F49620-96-1-0064). E.A.C. also thanks the Camille and Henry Dreyfus Foundation for support. We would like to thank Dr. Niranjan Govind and Dr. Stuart Watson for valuable discussions and comments during this work.

*Electronic address: asbjorn@chem.ucla.edu
†Electronic address: eac@chem.ucla.edu

[1] Y. H. Sohn, R. R. Biederman, and R. D. Sisson, Jr., Thin Solid Films **250**, 1 (1994).
[2] K. T. Wan, C. B. Khouw, and M. E. Davis, J. Catal. **158**, 311 (1996).
[3] F. Audry, P. E. Hoggan, J. Saussey, J. C. Lavalley, H. Lauron-Pernot, and A. M. Le Govic, J. Catal. **168**, 471 (1997).
[4] A. Trovarelli, F. Zamar, J. Llorca, C. de Leitenburg, G. Dolcetti, and J. T. Kiss, J. Catal. **169**, 490 (1997).
[5] W. Stichert and F. Schüth, J. Catal. **174**, 242 (1998).
[6] C. N. R. Rao, B. C. Satishkumar, and A. Govindaraj, Chem.

Commun. (Cambridge) **1997**, 1581 (1997).
[7] K.-O. Axelsson, K.-E. Keck, and B. Kasemo, Appl. Surf. Sci. **25**, 217 (1986).
[8] I. Birkby, P. Harrison, and R. Stevens, J. Eur. Ceram. Soc. **5**, 37 (1989).
[9] D. Majumdar and D. Chatterjee, Thin Solid Films **206**, 349 (1991).
[10] N. K. Huang, J. Mater. Sci. Lett. **11**, 681 (1992).
[11] G. S. A. M. Theunissen, A. J. A. Winnubst, and A. J. Burggraaf, J. Mater. Sci. **27**, 5057 (1992).
[12] C. Morterra, G. Cerrato, L. Ferroni, A. Negro, and L. Montanaro, Appl. Surf. Sci. **65/66**, 257 (1993).
[13] C. Morterra, G. Cerrato, L. Ferroni, and L. Montanaro, Mater. Chem. Phys. **37**, 243 (1994).
[14] L. E. Depero, R. Bertoncello, T. Boni, P. Levrangi, I. Natali Sora, E. Tempesti, and F. Parmigiani, J. Mater. Res. **12**, 1376 (1997).
[15] G. Cerrato, S. Bordiga, S. Barbera, and C. Morterra, Surf. Sci. **377–379**, 50 (1997); Appl. Surf. Sci. **115**, 53 (1997).
[16] A. J. A. Winnubst, P. J. M. Kroot, and A. J. Burggraaf, J. Phys. Chem. Solids **44**, 955 (1983).
[17] J. S. Solomon and J. T. Grant, J. Vac. Sci. Technol. A **3**, 373 (1985).
[18] M. Cotter and R. G. Egdell, J. Solid State Chem. **66**, 364 (1987).
[19] R. Orlando, C. Pisani, E. Ruiz, and P. Sautet, Surf. Sci. **275**, 482 (1992).
[20] N. I. Medvedeva, V. P. Zhukov, M. Ya. Khodos, and V. A. Gubanov, Phys. Status Solidi B **160**, 517 (1990).
[21] H. J. F. Jansen, Phys. Rev. B **43**, 7267 (1991). In Table I in this reference the remaining 0.1 electrons/unit cell in the O($2s$) band is represented by the O($3d$) orbitals, which is not included in Table I in this reference (private communication).
[22] R. H. French, S. J. Glass, F. S. Ohuchi, Y.-N. Xu, and W. Y. Ching, Phys. Rev. B **49**, 5133 (1994).
[23] L. Soriano, M. Abbate, J. Faber, C. Morant, and J. M. Sanz, Solid State Commun. **93**, 659 (1995); L. Soriano, M. Abbate, J. C. Fuggle, M. A. Jiménez, J. M. Sanz, C. Mythen, and H. A. Padmore, *ibid.* **87**, 699 (1993).
[24] L. L. Boyer and B. M. Klein, J. Am. Ceram. Soc. **68**, 278 (1985).
[25] E. V. Stefanovich, A. L. Shluger, and C. R. A. Catlow, Phys. Rev. B **49**, 11 560 (1994).
[26] M. Wilson, U. Schönberger, and M. Finnis, Phys. Rev. B **54**, 9147 (1996).
[27] A. W. Adamson and A. P. Gast, *Physical Chemistry of Surfaces* (Wiley, New York, 1997).
[28] Y.-M. Juan and E. Kaxiras, Phys. Rev. B **48**, 14 944 (1993).
[29] J. Goniakowski, J. M. Holender, L. N. Kantorovich, M. J. Gillan, and J. White, Phys. Rev. B **53**, 957 (1996).
[30] D. Sotiropoulou and P. Nikolopoulos, J. Mater. Sci. **26**, 1395 (1991).
[31] A. Tsoga and P. Nikolopoulos, J. Mater. Sci. **31**, 5409 (1996).
[32] J. D. McCullough and K. N. Trueblood, Acta Crystallogr. **12**, 507 (1959).
[33] G. Teufer, Acta Crystallogr. **15**, 1187 (1962).
[34] O. Ruff and F. Ebert, Z. Anorg. Allg. Chem. **180**, 19 (1929).
[35] M. C. Payne, M. P. Teter, D. C. Allen, T. A. Arias, and J. D. Joannopoulos, Rev. Mod. Phys. **64**, 1045 (1992). The computer code CASTEP is distributed and maintained by Molecular Simulations Inc.
[36] H. L. Skriver and N. M. Rosengaard, Phys. Rev. B **46**, 7157 (1992).
[37] M. Methfessel, D. Hennig, and M. Scheffler, Phys. Rev. B **46**, 4816 (1992).
[38] V. I. Anisimov and F. Aryasetiawan, J. Phys.: Condens. Matter **9**, 767 (1997).
[39] C. Noguera, *Physics and Chemistry at Oxide Surfaces* (Cambridge University Press, Cambridge, 1996).
[40] M. Morinaga, H. Adachi, and M. Tsukada, J. Phys. Chem. Solids **44**, 301 (1983).
[41] J. M. Sanz, A. R. González-Elipe, A. Fernández, D. Leinen, L. Galán, A. Stampfl, and A. M. Bradshaw, Surf. Sci. **307/309**, 848 (1994).
[42] N. Troullier and J. L. Martins, Phys. Rev. B **43**, 1993 (1991).
[43] W. C. Topp and J. J. Hopfield, Phys. Rev. B **7**, 1295 (1973).
[44] D. M. Ceperley and B. J. Alder, Phys. Rev. Lett. **45**, 566 (1980).
[45] J. Perdew and A. Zunger, Phys. Rev. B **23**, 5048 (1981).
[46] L. Kleinman and D. M. Bylander, Phys. Rev. Lett. **48**, 1425 (1982).
[47] S. Pugh and M. J. Gillan, Surf. Sci. **320**, 331 (1994).
[48] M. A. Szymański and M. J. Gillan, Surf. Sci. **367**, 135 (1996).
[49] J. Goniakowski and M. J. Gillan, Surf. Sci. **350**, 145 (1996).
[50] C. Leung, M. Weinert, P. B. Allen, and R. M. Wentzcovitch, Phys. Rev. B **54**, 7857 (1996).
[51] The CERIUS^2 software package and the CASTEP code is distributed and maintained by Molecular Simulations Inc.
[52] J. S. Lin, A. Qteish, M. C. Payne, and V. Heine, Phys. Rev. B **47**, 4174 (1993).
[53] G. P. Francis and M. C. Payne, J. Phys.: Condens. Matter **2**, 4395 (1990).
[54] R. Stevens, *Zirconia and Zirconia Ceramics* (Magnesium Elektron Ltd., Twickenham, England, 1986).
[55] P. Aldebert and J.-P. Traverse, J. Am. Ceram. Soc. **68**, 34 (1985).
[56] H. G. Scott, J. Mater. Sci. **10**, 1527 (1975).
[57] A. M. Rappe, K. M. Rabe, E. Kaxiras, and J. D. Joannopoulos, Phys. Rev. B **41**, 1227 (1990).
[58] D. Vanderbilt, Phys. Rev. B **41**, 7892 (1990).
[59] K. Takayanagi, Y. Tanishiro, M. Takahashi, and S. Takahashi, J. Vac. Sci. Technol. A **3**, 1502 (1985).
[60] M. Schönnenbeck, D. Cappus, J. Klinkmann, H.-J. Freund, L. G. M. Petterson, and P. S. Bagus, Surf. Sci. **347**, 337 (1996).
[61] N. Ting, Y. Qingliang, and Y. Yiying, Surf. Sci. **206**, L857 (1988).
[62] S. P. Bates, G. Kresse, and M. J. Gillan, Surf. Sci. **385**, 386 (1997).
[63] F. Zandiehnadem, R. A. Murray, and W. Y. Ching, Physica B **150**, 19 (1988).
[64] V. E. Henrich and P. A. Cox, *The Surface Science of Metal Oxides* (Cambridge University Press, Cambridge, 1994).
[65] R. C. Garvie, R. H. Hannink, and R. T. Pascoe, Nature (London) **258**, 703 (1975).
[66] R. C. Garvie and M. F. Goss, J. Mater. Sci. **21**, 1253 (1986); R. C. Garvie, J. Phys. Chem. **69**, 1238 (1965); **82**, 218 (1978).
[67] G. H. Bansil and A. H. Heuer, Acta Metall. **20**, 1281 (1972).
[68] G. K. Bansil and A. H. Heuer, Acta Metall. **22**, 409 (1974).
[69] A. R. Miedema, P. F. de Châtel, and F. R. de Boer, Physica B **100**, 1 (1980); F. R. de Boer, R. Boom, W. C. M. Mattens, A. R. Miedema, and A. K. Niessen, *Cohesion in Metals* (North-Holland, Amsterdam, 1988).